

Non-Linear Stiffness Extraction & Modeling of Wineglass Disk Resonators

*Alain Anton
Clark Nguyen, Ed.*



Electrical Engineering and Computer Sciences
University of California at Berkeley

Technical Report No. UCB/EECS-2018-183

<http://www2.eecs.berkeley.edu/Pubs/TechRpts/2018/EECS-2018-183.html>

December 14, 2018

Copyright © 2018, by the author(s).
All rights reserved.

Permission to make digital or hard copies of all or part of this work for personal or classroom use is granted without fee provided that copies are not made or distributed for profit or commercial advantage and that copies bear this notice and the full citation on the first page. To copy otherwise, to republish, to post on servers or to redistribute to lists, requires prior specific permission.

Non-Linear Stiffness Extraction & Modeling of Wineglass Disk Resonators

by Alain Antón

Research Project

Submitted to the Department of Electrical Engineering and Computer Sciences, University of California at Berkeley, in partial satisfaction of the requirements for the degree of **Master of Science, Plan II**.

Approval for the Report and Comprehensive Examination:

Committee:

Professor Clark T.C. Nguyen

Research Advisor

(Date)

* * * * *

Professor Michel Maharbiz

Second Reader

(Date)

Non-Linear Stiffness Extraction & Modeling of Wineglass Disk Resonators

by Alain Antón

Committee:

Professor Clark T.C. Nguyen, Research Advisor

Professor Michel Maharbiz, Second Reader

For those I value most in my life, my family

Abstract

Non-Linear Stiffness Extraction & Modeling of Wineglass Disk Resonators

by

Alain Antón

Master of Science in Electrical Engineering and Computer Sciences

University of California, Berkeley

Professor Clark T.-C. Nguyen

Over the past three to four decades the popularity of MEMS has continually grown with the development of different technologies ranging from thin film bulk acoustic resonators (FBAR), to capacitive gap transducers, and surface acoustic wave (SAW) resonators, just to name a few. Each of which has their own benefits and drawbacks when considering different applications, say sensors or radio frequency (RF) front end components. For example, the prevalent use of FBAR in consumer electronics for RF wideband filters is largely due to the technology's ability to suppress spurious modes, temperature stability, and high coupling coefficient (k_t^2). However, for the implementation of channel select filters, low phase noise and low power oscillators, and RF switches (or Resoswitches), capacitive gap transducers are desirable because of their low loss, high quality factor characteristics. Where the quality factor of a typical FBAR device at 2GHz sits at around 2,000, that of a capacitive gap transducer operating at 2.97 GHz sits at about 42,900. However, devices with very high quality factors approach their non-linear mode of operation at much lower input powers (drive voltages) in comparison to their low-quality factor counter parts. Thus, in this report, we employ the harmonic balance method to present a robust non-linear analytical model to study device behavior at high input powers.

We extract the mechanical non-linear stiffness, k_{m3} , of a 61 MHz wineglass disk (WGD) to be 126.53 pN/nm³ by fitting typical device through measurements to the derived model. Additionally, we derive an analytical approximation to the non-linear electrical stiffness, k_{e3} , by taking up to the fourth term in the Taylor series expansion of $\partial C / \partial r$. While this approximation serves as a reliable calculation, to solve for the exact solution of k_{e3} , requires more experimentation. Lastly, we accurately predict and demonstrate the bias voltage, $V_{P_{crit}}$, that eliminates non-linear behavior (both spring softening and hardening) to be 7.9079 V for the 61 MHz WGD in this work.

Professor Clark T.-C. Nguyen
Research Advisor

Table of Contents

Chapter 1: Introduction	1
1.1 Background and Objective.....	1
1.2 Overview.....	2
Chapter 2: Resonator Theory and Operation.....	3
2.1 Governing Equation of Motion.....	3
2.2 Measured Displacement Amplitude.....	6
2.3 Electrode to Resonator Gap (<i>do</i>).....	7
2.4 Resonator Input Voltage (<i>vi</i>).....	8
2.5 Linear Analytical Model vs. Measurement.....	10
Chapter 3: Duffing Theory and Operation	12
3.1 Harmonic Balance Frequency Response Solution.....	12
3.2 Fitting Measurement to Duffing Model.....	14
3.3 Non-Linear Electrical and Mechanical Stiffnesses (<i>ke3, km3</i>)	15
Chapter 4: Conclusion.....	18
4.1 Achievements.....	18
4.2 Future Research Directions.....	18
Appendix A: Non-Linear Model Curve Fits	19
References.....	21

Table of Figures

Figure 1: SEM of 61 MHz WGD.....	1
Figure 2: Test Set Up and Physical Parameters	3
Figure 3: Device Mode Shape.....	4
Figure 4: S21 Measurements at varied bias voltages, VP	7
Figure 5: Measured and fitted resonant frequency, f_o , as a function of bias voltage, VP	8
Figure 6: Measured and fitted quality factors, Q , as a function of total resistance R_{total}	9
Figure 7: Measured and fitted vibration spectrum in the linear mode of operation	10
Figure 8: Non-linear measured data and model (VP = 15 V and Pin, dBm = -14 dBm).	14
Figure 9: Non-Linear stiffness, k3 , as a function of bias voltage, VP	16
Figure 10: Normalized vibration amplitude with spring softening and nullification	17
Figure 11: Non-linear measured data and model (VP = 9 V and Pin, dBm = -10 dBm).	19
Figure 12: Non-linear measured data and model (VP = 13 V and Pin, dBm = -10 dBm)	19
Figure 13: Non-linear measured data and model (VP = 14 V and Pin, dBm = -14 dBm)	20
Figure 14: Non-linear measured data and model (VP = 10 V and Pin, dBm = -14 dBm)	20

Acknowledgements

First and foremost, I would like to express my utmost gratitude to my advisor Clark T.C. Nguyen. His guidance, immense depth of knowledge and wisdom have shaped me into a much better researcher throughout these past two and a half years. I will never forget all the personal and academic guidance he has provided. It was always a fun time meeting with Clark, I could never tire of his nonchalant sense of humor and long conversations about topics loosely related to research. Most importantly, I am thankful for his patience, and respect toward his students. You will be missed Clark!

A big thanks to professor Michele Maharbiz for being a mentor for the last year. It was great to hear your perspective and advise as a fellow Miamian. Thanks for being straight forward with me and putting reality in perspective.

To my friends; Kieran Peleaux, Phong Nguyen, Kyle Tanghe, and Qianyi Xie. Thank you so much for being there with me during all those long days and nights filled with research, studying, classwork, projects, lack of sleep, and coffee. Sharing all these experiences have brought us closer together on a personal level and it has been a great ride along you guys. Thanks for all conversations and discussions that helped shape this research project.

A special thanks to Shirley, who does a fantastic job in helping all the graduate students in the department and is always there for support. Thanks to the BSAC staff who always put in a lot of work in setting up the IAB sessions every semester. Thanks to all the previous student's in Clark's research group who have done extraordinary research and paved the way for me to complete this report. Thanks to Zeying Ren for fabricating the amazing devices used in this work.

Lastly, I am extremely grateful and indebted to my family who have sacrificed so much for me to be where I am today. Without them, I would not have the phenomenal opportunities available to me in this country. I hope I have made them proud, because this can only serve as a small token of my gratitude for what they have done for me.

Chapter 1: Introduction

1.1 Background and Objective

Over the past three to four decades the popularity of MEMS has continually grown, with the development of different technologies ranging from thin film bulk acoustic resonators (FBAR) [1], to capacitive gap transducers [2], and surface acoustic wave (SAW) resonators [3], just to name a few. Each of which has their own benefits and drawbacks when considering different applications, say sensors or radio frequency (RF) front end components. For example, the prevalent use of FBAR in consumer electronics for RF wideband filters is largely due to the technology's ability to suppress spurious modes, temperature stability, and high coupling coefficient (k_t^2). However, for the implementation of channel select filters, low phase noise and low power oscillators, and RF switches (or Resoswitches), capacitive gap transducers are desirable because of their low loss, high

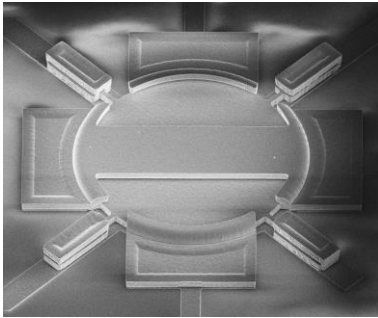


Figure 1: SEM of 61 MHz WGD

quality factor characteristics. Where the quality factor of a typical FBAR device at 2GHz sits at around 2,000 [4] and that of a capacitive gap transducer operating at 2.97 GHz sits at about 42,900 [5]. However, with very high quality factors, devices approach their non-linear mode of operation at much lower input powers (drive voltages) in comparison to their low-quality factor counter parts. Thus, non-linearity mitigation techniques for high Q capacitive gap transducers would enable

linear device operation at higher input powers.

In this report we analyze the linear and non-linear behavior of a 61 MHz wineglass disk resonator (WGD), Figure 1, fabricated using the process flow described in [6] in 2009. The structural, interconnect, and electrode layers are composed of doped polysilicon to achieve high and reliable quality factors. Note from Figure 1, that there is a large overhang connecting two of the four electrodes together. This connection serves as one port (input/output) and, although not pictured, there is a second connection between electrodes routed through the interconnect layer to serve as the second port (input/output). Lastly the device structure also has routing for a biasing port. These three ports provide enough access to the device for a proper through measurement using a network analyzer and a power supply.

1.2 Overview

This report applies established methods [6] [7] [8] to successfully extract and model the nonlinear mechanical and electrical stiffnesses of a WGD resonator to instill design intuition to maintain linear operation.

In Chapter 2 we cover a brief review on the basic theory and operation of a 61 MHz WGD. Including derivations of related equations, an analytical linear model, and extraction of non-measurable parameters.

In Chapter 3 we expand on the linear model derived in Chapter 2 to include non-linearities at high vibration amplitudes due to non-linear stiffnesses. We fit duffing measured data to this model and validate its accuracy to predict device behavior.

Finally, Chapter 4 concludes this work with an overall summary of the work presented and a path for future research.

Chapter 2: Resonator Theory and Operation

The governing equations in the typical mode of operation will be briefly reviewed as they have been derived in previous works [9] [6] [10] [11]. Figure 2 shows a perspective view of a 61 MHz WGD connected to all the necessary test equipment to perform a two-port measurement. Additionally, also included, in Figure 2 are important physical parameters such as resonator thickness, radius, electrode to disk gap spacing, the electrodes' overlap angle, and axes (t, R_{disk}, d_o, ϕ_k respectively).

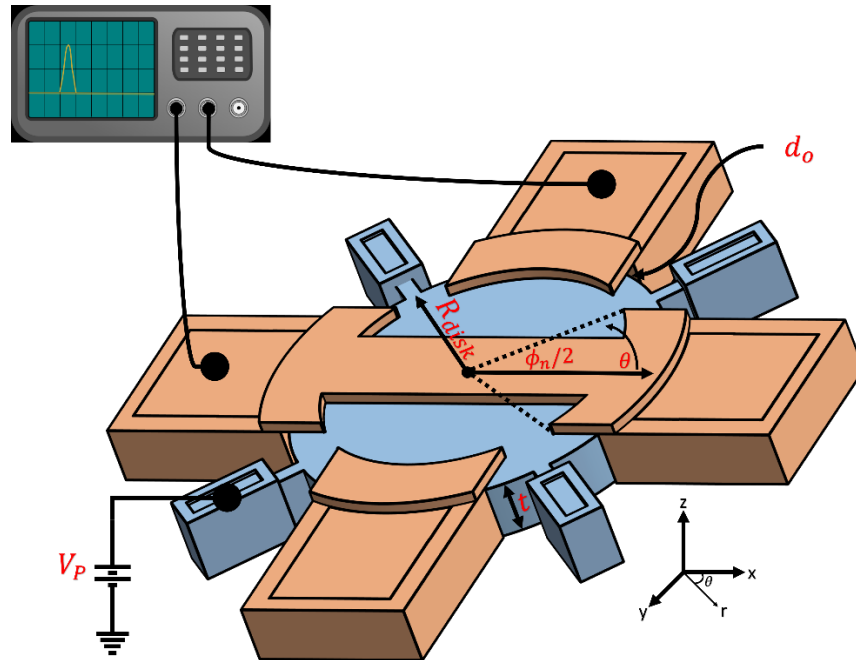


Figure 2: Test Set Up and Physical Parameters

2.1 Governing Equation of Motion

Applying a direct current (DC) voltage, V_P , on the structure and an alternating current (AC) voltage, v_i , at the input of the device, as seen on Figure 2, generates a radial electrostatic force, F_{es} , given by [9]:

$$F_{es} = \frac{1}{2} \left(\frac{\partial C_k}{\partial r} \right) (V_P - v_i)^2 \quad (1)$$

where the electrode to disk overlap capacitance is:

$$C_k(r) = \frac{\epsilon_o \phi_k R_{disk} t}{d_o - r} \rightarrow \left(\frac{\partial C_k}{\partial r} \right) = \frac{C_{ok}}{d_o} \left(1 - \frac{r}{d_o} \right)^{-2} \quad (2)$$

where C_{ok} , and ϵ_o are respectively the static electrode to resonator capacitance at the k^{th} port and the permittivity of free space. The expression in the right hand side of (2) can be expanded with a Taylor series into the more common form of [10]:

$$\left(\frac{\partial C_k}{\partial r} \right) = \frac{C_{ok}}{d_o} \cdot \sum_{n=0}^N \frac{(n+1)\alpha_n r^n}{d_o^n} \quad (3)$$

where the introduction of the modification factor, α_n , in (3) correctly modifies the change in capacitance per unit displacement, $\left(\frac{\partial C_k}{\partial r} \right)$, of an ideal parallel plate capacitive gap transducer to account for a non-constant near-resonance displacement. The modification factor for the first two terms of the Taylor series expansion, α_0 and α_1 , were proven to be, κ_k and κ_k^2 [6]:

$$\kappa_k = \frac{1}{(\theta_{k2} - \theta_{k1})} \int_{\theta_{k1}}^{\theta_{k2}} \frac{\mathcal{R}_{mode}(R_{disk}, \theta)}{\mathcal{R}_{mode}(R_{disk}, \phi_{core})} \cdot d\theta \quad (4)$$

where $\theta_{k2} = -\theta_{k1} = \frac{\phi_k}{2} = 38.5^\circ$, $\phi_{core} = 0^\circ$ (the angle where the WGD displacement is at a maximum) and $\mathcal{R}_{mode}(R_{disk}, \theta)$ alongside $\mathcal{R}_{mode}(R_{disk}, \phi_{core})$ are the displacements at the edge of the disk at angles θ (integrating over) and ϕ_{core} respectively. The expression for $\mathcal{R}_{mode}(r, \theta)$ is in [6].

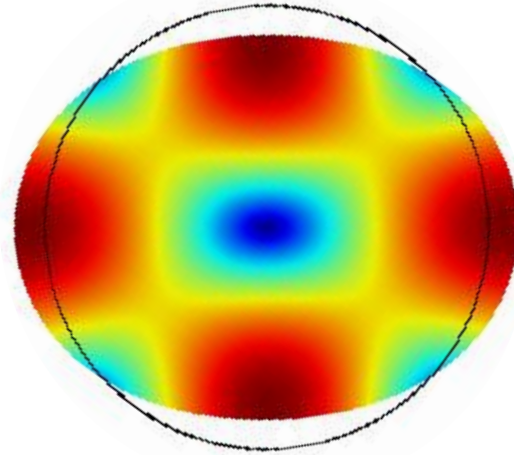


Figure 3: Device Mode Shape

Modeling the linear operation of the device only requires the first two terms of (3). Taking these two terms and plugging them into (1) brings us to:

$$F_{es,lin} = \frac{1}{2} \frac{\kappa_k C_{ok}}{d_o} \left(1 + \frac{2\kappa_k}{d_o} r \right) (V_P - v_i)^2 \quad (5)$$

With some algebraic manipulations, and leaving terms only at the frequency of v_i , the electrostatic force simplifies to:

$$F_{es,lin} \approx -\frac{\kappa_k V_P v_i C_{ok}}{d_o} + \frac{\kappa_k^2 V_P^2 C_{ok}}{d_o^2} r \quad (6)$$

the second force term has a coefficient directly proportional to the radial motion of the device. Remembering Hooke's Law, we note that this coefficient is a stiffness, commonly known as the electrical stiffness, k_{e1k} :

$$k_{e1k} = \frac{\kappa_k^2 V_P^2 C_{ok}}{d_o^2} \quad (7)$$

Inserting the electrostatic force (6) into the spring-mass-damper equation of motion and moving the electrical stiffness term to the other side leads us to the following governing differential equation of motion for the WGD:

$$m_m \ddot{r} + b_m \dot{r} + (k_{m1} - k_{e1})r = F_{in} \quad (8)$$

where F_{in} is the first term of (6). Values for the resonator motional mass (m_m), damping coefficient (b_m), and linear stiffness (k_{m1}) are in Table I. Equations and procedures to obtain said values are in [6]:

Using the phasor form of (8), and solving for the displacement amplitude magnitude as a function of frequency, brings us to:

$$|r| = \frac{|F_{in}|}{\left[((k_{m1} - k_{e1}) - m_m \omega^2)^2 + (b\omega)^2 \right]^{\frac{1}{2}}} \quad (9)$$

2.2 Measured Displacement Amplitude

We would like to compare this linear analytical model, (9), with measured data gathered from the set up pictured in Figure 2. To do this we must convert the S_{21} data gathered to the WGD's displacement amplitudes. We start off by noting that the output current at port 2, i_{o_2} , is dependent on both the voltage and time (τ) varying capacitance across the 2^{nd} electrode to resonator gap and is therefore [6]:

$$|i_{o_2}| = V_p \left(\frac{\partial C_2}{\partial \tau} \right) = V_p \left(\frac{\partial C_2}{\partial r} \right) \left(\frac{\partial r}{\partial \tau} \right) = \omega \kappa_2 V_p \frac{C_{o_2}}{d_o} |r|_{meas} \quad (10)$$

to calculate the measured current at port 2 of the network analyzer we make use of the following equations:

$$S_{21} = 10 \log \left(\frac{P_{out}}{P_{in}} \right) \rightarrow P_{out} = P_{in} 10^{\frac{S_{21}}{10}} \quad (11)$$

where P_{out} and P_{in} are, respectively, the power measured at port two of the network analyzer and the power delivered by port one of the network analyzer. The delivered power, P_{in} , in its linear form is:

$$P_{in} = 1mW \cdot 10^{\frac{P_{in,dBm}}{10}} \quad (12)$$

note that $P_{in,dBm}$ is manually set in the network analyzer.

$$P_{out} = I_{rms}^2 R_{out} = \frac{1}{2} |i_{o_2}|^2 R_{load} \quad (13)$$

where R_{load} is the port 2 impedance.

Using (11) - (13) we arrive at an equation for the measured displacement amplitude as a function of frequency and the corresponding S_{21} data:

$$|r|_{meas} = \frac{|i_{o_2}| d_o}{\omega \kappa_2 V_p C_{o_2}} = \sqrt{\frac{1mW \cdot 2 \cdot 10^{\frac{P_{in,dBm} + S_{21}}{10}}}{R_{out}}} \frac{d_o}{\omega \kappa_2 V_p C_{o_2}} \quad (14)$$

2.3 Electrode to Resonator Gap (d_o)

To be able to use either (9) or (14), we must obtain the electrode to resonator gap, d_o . One can express the resonance frequency of the WGD as:

$$\omega_o = \sqrt{\frac{k_{m1} - 4k_{e1}}{m_m}} \quad (15)$$

thus we can see that the electrical stiffness is pulling down the natural mechanical resonant frequency of the device as shown in previous works [9] [6] [10] [11]. Noting from (7), that the electrical stiffness is a function of V_p and d_o , we can measure the resonant frequency of the WGD as a function of V_p , as seen in Figure 4.

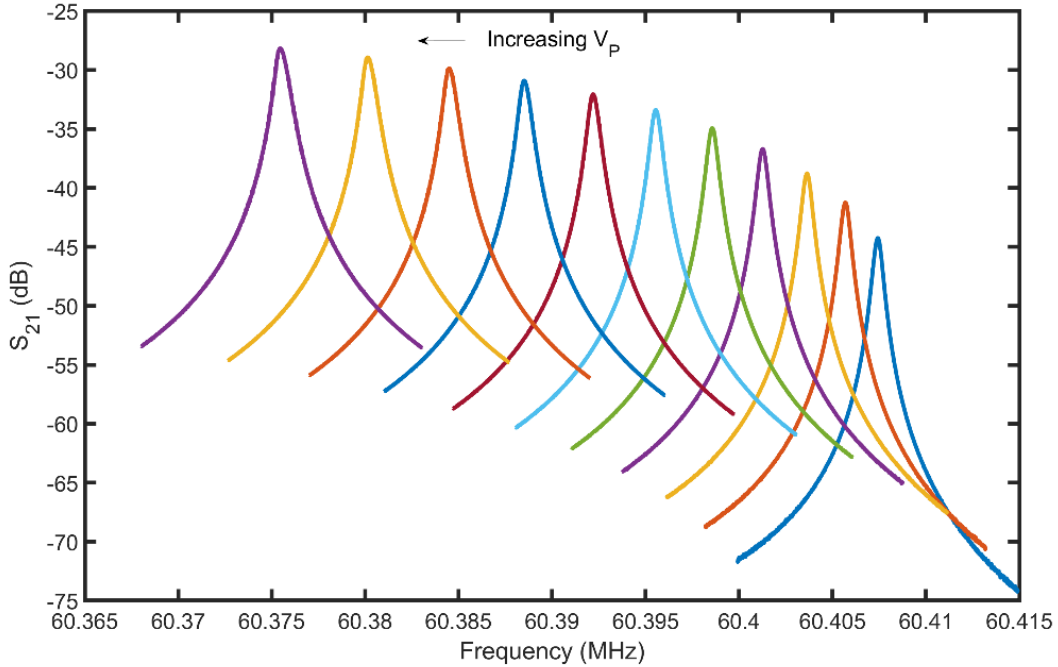


Figure 4: S_{21} Measurements at varied bias voltages, V_p

With the data gathered in Figure 4, we can plot the measured resonant frequency as a function of the bias voltage, V_p , and use the expression for the measured resonance frequency, f_{meas} :

$$f_{meas} = \frac{1}{2\pi} \sqrt{\frac{\left(k_m - 4 \cdot \frac{\kappa_2^2 V_p^2 \epsilon_o \phi_2 R t}{d_o^3}\right)}{m_m}} \quad (16)$$

to fit the data to the electrode to resonator gap, d_o , as shown in Figure 5.

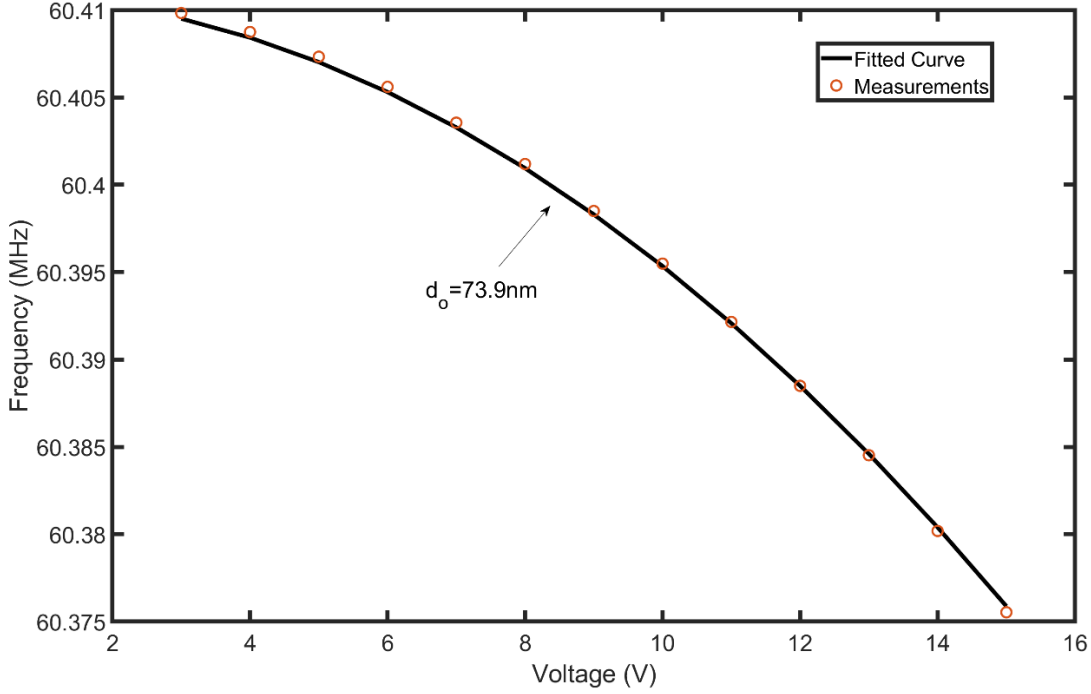


Figure 5: Measured and fitted resonant frequency, f_o , as a function of bias voltage, V_p

2.4 Resonator Input Voltage (v_i)

As mentioned in section 0, $P_{in,dBm}$ is manually set in the Network Analyzer, but this is the power the device under test (DUT) would receive if it was perfectly matched to the impedance of port one. Therefore, the network analyzer is sourcing a total power, P_{total} , of:

$$P_{total} = 2P_{in} \rightarrow P_{total,dBm} = P_{in,dBm} + 3 \text{ dB} \quad (17)$$

such that the DUT receives the programmed power under matched conditions. Since there is an impedance mismatch between the WGD and the network analyzer's port impedances, we must consider what the input voltage, v_i , is as a function of frequency to properly determine the input electrostatic force, F_{in} .

The impedance model of the WGD consists of a series resonant RLC circuit, with the expressions of each component given by [6]:

$$R_x = \frac{\sqrt{m_m k_m}}{Q \left(\frac{V_p \kappa_i C_o}{d_o} \right)^2} \quad L_x = \frac{m_m}{\left(\frac{V_p \kappa_i C_o}{d_o} \right)^2} \quad C_x = \frac{\left(\frac{V_p \kappa_i C_o}{d_o} \right)^2}{k_m - k_{e1}} \quad (18)$$

Note however, that the effective electrical resistance, R_x , is dependent on both the quality factor (Q) and bias voltage (V_p). Thus, at low bias voltages we observe higher quality factors, and decreasing quality factors as V_p increases because the electrical resistance of the device rapidly decreases as the bias voltage increases and loading from parasitics dominate. The expression for the loaded quality factor, Q_L , is:

$$Q_L = Q_o \frac{R_x}{R_x + R_p + R_{source} + R_{load}} = Q_o \frac{R_x}{R_x + R_y} \quad (19)$$

where Q_o , R_p , and R_{source} , are the intrinsic quality factor, total parasitic resistance, and source (port 1) resistance. From (19), we can observe a key detail, the quality factors observed in measurements are the loaded quality factors, hence the resistance calculated by using (18) is actually the sum of all resistances in series with the device (i.e. $R_x + R_y$). Since the calculated effective resistance includes parasitics (input and output ports as well), to solve for the input voltage we must first determine the parasitic resistances.

To solve for the parasitic resistance, we must plot the loaded quality factor as a function of effective resistance (i.e. bias voltage) and fit the data to (19) as shown in Figure 6.

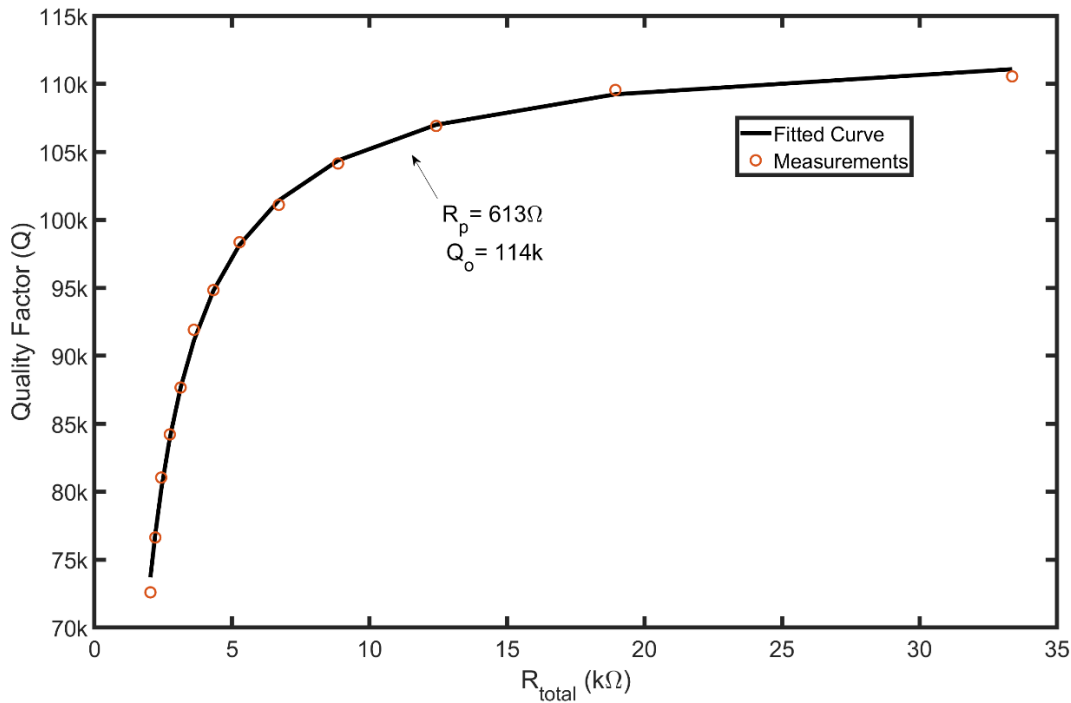


Figure 6: Measured and fitted quality factors, Q , as a function of total resistance R_{total}

The device resistance can be calculated now that we have obtained the parasitic resistances. Remembering that (18) provides the total series resistance R_{total} (i.e. $R_x + R_y$), we can obtain R_x by simply subtracting R_y , which we have all the values for. We now assume the WGD is perfectly symmetric (intended by design) and place half the parasitic resistances before the input and the other half after the output. In doing so, we can quickly analyze the circuit and retrieve the amplitude of the input voltage as:

$$|v_{in}| = 2\sqrt{2P_{in}R_{source}} \left(\frac{(R_x + R_{load} + \frac{1}{2}R_p)}{(R_x + R_{source} + R_{load} + R_p)} \right) \quad (20)$$

2.5 Linear Analytical Model vs. Measurement

Now that all necessary parameters have been extracted and our model is complete, we compare the measured response (14), and the analytical linear model (9), of the resonator. Figure 7 shows the measured response and the analytical response using the adjusted values provided in

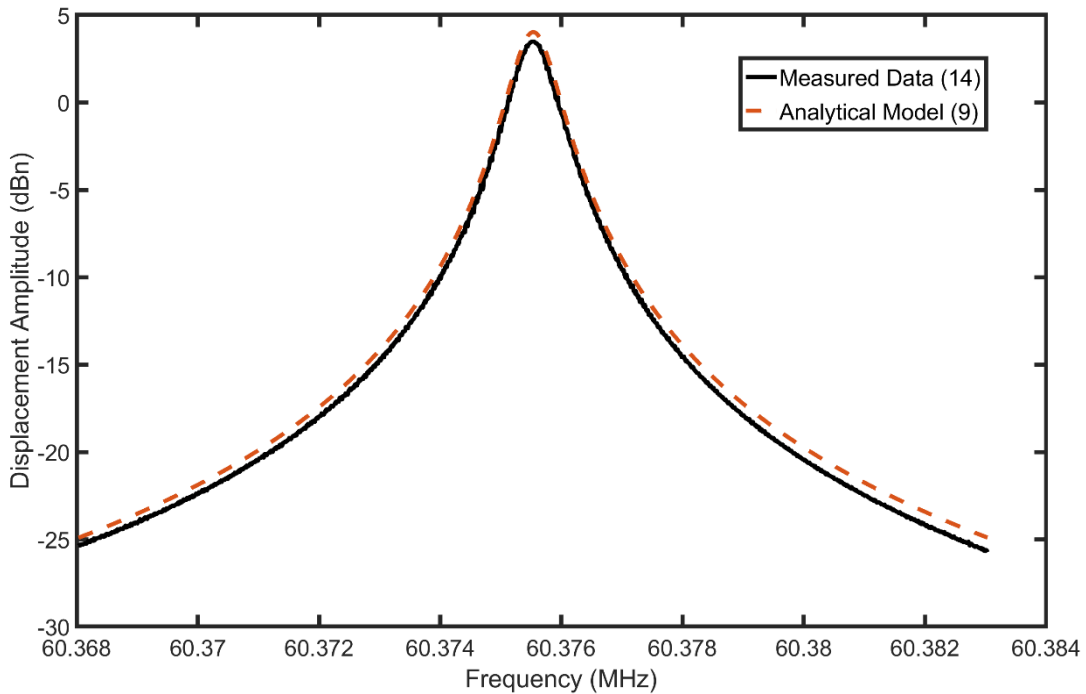


Figure 7: Measured and fitted vibration spectrum in the linear mode of operation

The linear model matches the measured data well even though it does not include other parasitic feedthrough paths and capacitances. A more involved circuit model demonstrated in [6] adequately models all the different parasitics present in the device.

Table I: WGD Design and Performance Summary

	Parameter	Design Source	Design	Measured	Adjusted	Unit
Material Constants	Young's Modulus, E	Process	158	-	158	GPa
	Density, ρ	Process	2300	-	2300	kg/m ³
	Frequency Material Constant, K_{mat}	[6]	0.476	-	0.476	-
WGD Parameters	Mechanical Resonant Frequency, f_{nom}	Spec.	60.06	60.41	-	MHz
	WGD Radius, R_{disk}	Layout	32	31.82	31.82	μm
	Structural Material Thickness, t	Process	3	3	3	μm
	Electrode Span Angle, ϕ	Layout	77.2	77.2	77.2	$^\circ$
	Resonant Quality Factor, Q	Process	75,000	72,598	72,598	-
	Dynamic Mass at ϕ_{core} , m_m	[6]	8.04	-	8.08	ng
	Dynamic Stiffness at ϕ_{core} , k_m	[6]	1.15	-	1.16	mN/nm
	Dynamic Damping at ϕ_{core} , b_m	[6]	41.8	-	42.3	$\mu\text{g/s}$
	Electrical Stiffness, k_{e1}	(7)	394	-	1.35	$\mu\text{N/nm}$
	Electrode to Resonator Gap, d_o	Process	70	-	73.6	nm
Lumped Circuit Elements	Total Parasitic Resistance, R_p	Process	0	600	600	Ω
	Resonator Effective Resistance, R_x	(18)	6.5	-	7.97	k Ω
	Resonator Effective Capacitance, C_x	(18)	5.63	-	4.56	aF
	Resonator Effective Inductance, L_x	(18)	1.25	-	1.52	H
Test Equipment Parameters	DC Bias Voltage, V_p	Test Setup	15	15	15	V
	NA Power $P_{in,dBm}$	Test Setup	-40	-40	-40	dBm
	NA Port 1 Resistance, R_{source}	Test Setup	50	50	50	Ω
	NA Port 2 Resistance, R_{load}	Test Setup	50	50	50	Ω

*Boldface values indicate adjustment to match measured data

Chapter 3: Duffing Theory and Operation

Non-linear behavior in the WGD at high vibration amplitudes deviates the operation of the device from the linear model derived in Section 2.1. The forced Duffing equation:

$$m_m \ddot{r} + b_m \dot{r} + k_1 r + k_2 r^2 + k_3 r^3 = F_{in} \quad (21)$$

describes the WGD non-linear operation analogously to how (9) describes the linear mode of operation. There have been various demonstrations of methods to arrive at an analytical solution to (21). These methods include, but are not limited to, the multiple scales method [12], averaging method [13], homotopy analysis method (HAM) [14] and the harmonic balance method [8] [7]. The first two methods are known to produce accurate solutions for weakly non-linear problems, while the latter two serve as more suitable methods for strongly non-linear problems [14]. Therefore, we employ the harmonic balance method due to its simplicity, frequency response solution, and ability to accurately model strongly non-linear problems.

3.1 Harmonic Balance Frequency Response Solution

We start off by assuming a first order sinusoidal solution to (21) in the form of:

$$r = x \cos(\omega t) + y \sin(\omega t) = r \cos(\omega t + \phi) \quad (22)$$

where

$$r^2 = x^2 + y^2 \quad , \quad \phi = \tan^{-1} \left(\frac{y}{x} \right) \quad (23)$$

From here we plug (22) into (21) and expand the nonlinear terms. Recall, that to generate an input electrostatic force, F_{in} , a sinusoidal input voltage, v_{in} , at frequency ω is necessary. Therefore, we are only interested in observing the frequency response at ω and consequently ignore higher harmonics and terms at DC. In doing so, we observe that the cubic term generates a harmonic at 3ω as well as a term at ω . Therefore, the third order nonlinear stiffness, k_3 , contributes one term to the frequency response of the device. However, the quadratic term generates a harmonic at 2ω and a term at DC and thus does not contribute anything at ω .

After expanding and truncating the terms to only those at ω , we group the coefficients of cosine and the sine and arrive at:

$$\begin{aligned} \cos(\omega t) \left[-mx\omega^2 + b_my\omega + k_1x + \frac{3}{4}k_3x^3 + \frac{3}{4}k_3xy^2 - F_{in} \right] \\ + \sin(\omega t) \left[-my\omega^2 - b_mx\omega + k_1y + \frac{3}{4}k_3y^3 + \frac{3}{4}k_3yx^2 \right] = 0 \end{aligned} \quad (24)$$

note that F_{in} driven as a cosine or a sine and it will not change the result. To satisfy (24) the coefficients of the cosine and sine must both be equal to zero and thus bring us to the two conditions:

$$-mx\omega^2 + b_my\omega + k_1x + \frac{3}{4}k_3x^3 + \frac{3}{4}k_3xy^2 = F_{in} \quad (25)$$

$$-my\omega^2 - b_mx\omega + k_1y + \frac{3}{4}k_3y^3 + \frac{3}{4}k_3yx^2 = 0 \quad (26)$$

squaring (25) and (26) then adding them together simplifies to:

$$\frac{1}{16}(x^2 + y^2)[(3k_3(x^2 + y^2) + 4k_1 - 4m_m\omega^2)^2 + 16(b_m\omega)^2] = F_{in}^2 \quad (27)$$

plugging r from (23) into (27) and algebraically simplifying concludes in:

$$r^2 \left[\left(\frac{3}{4}k_3r^2 + k_1 - m_m\omega^2 \right)^2 + (b_m\omega)^2 \right] = F_{in}^2 \quad (28)$$

Two details to note, if $k_1 - m\omega^2 \gg \frac{3}{4}k_3r^2$ (i.e. at small vibration amplitudes) we can solve for $|r|$ and (28) reduces to (9). Second, the linear and cubic stiffnesses, k_1 and k_3 respectively, include the mechanical and electrical stiffnesses, and thus:

$$k_1 = k_{m1} - k_{e1} \quad k_3 = k_{m3} - k_{e3} \quad (29)$$

where k_{m1} is in [6] and k_{e1} is given by (7). There are currently no analytical expressions for the WGD's nonlinear mechanical stiffness k_{m3} , but we will develop some intuition behind the nonlinear electrical stiffness k_{e3} in Section 3.3 and discuss a method in how to extract k_{m3} from data.

3.2 Fitting Measurement to Duffing Model

As of this writing, there is no accurate analytical expression for the non-linear stiffnesses of the WGD. Hence, we curve fit measured data, using (14), to the duffing analytical model (28) to extract the effective non-linear stiffness k_3 . Doing so, produces the plot shown in Figure 8 **Error! Reference source not found.** Note that more examples of non-linear fits are in demonstrated in Appendix A.

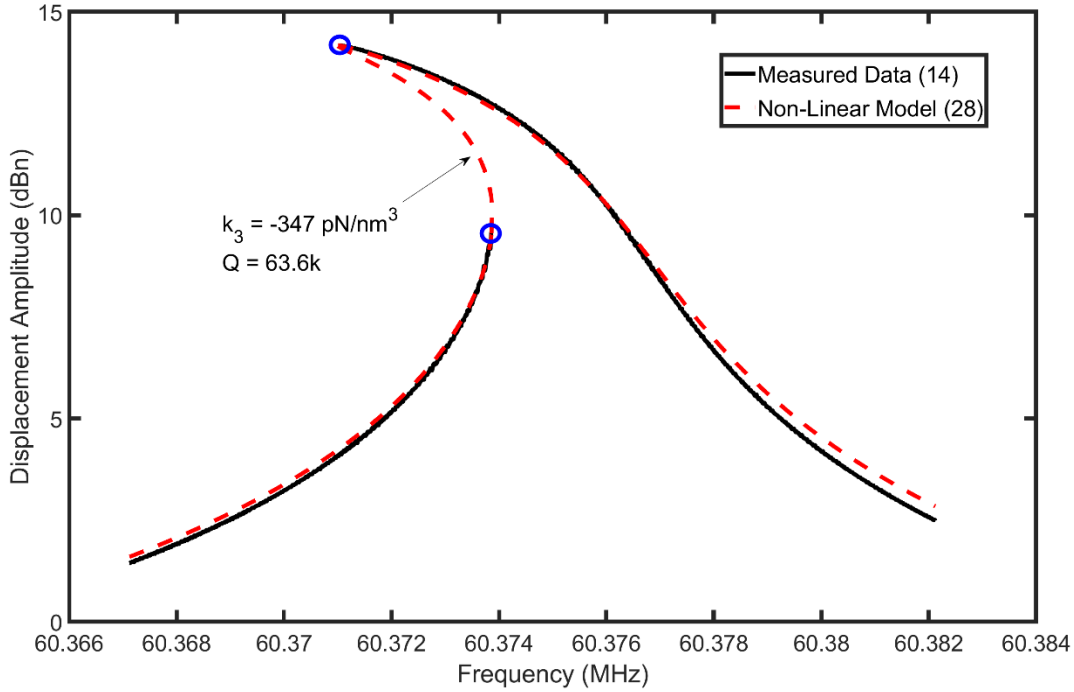


Figure 8: Non-linear measured data and model ($V_p = 15$ V and $P_{in,dBm} = -14$ dBm)

A few details to note, to generate the measured trace in Figure 8 we take two measurements: the first, by sweeping from low to high frequency and second, by sweeping from high to low frequency. This allows us to isolate each unstable point (blue circles in figure 8) and show the region of instability by combining the measurement data from both sweeps. A recent work [15], demonstrates the measurement of what we observe here as the instability region with a closed loop system by taking advantage of the one to one relationship between phase and both frequency and amplitude. This relationship allows the authors to perfectly recreate the amplitude-to-frequency spectrum without the instability region, which therefore implies their perspective resonator is stable within that range of frequencies. However, for the purpose of this work, extracting and plotting the unstable points provides enough information to test our model and extract k_3 . Additionally, the effective Q to properly match the measured data to the model is smaller than that of the device operating at lower input powers, which in theory should be the same. We cannot measure the Q of the device in the duffing mode of operation since part of the -3dB bandwidth

falls within the region of instability. Therefore, we cannot compare the measured Q to that of the fitted value. Appendix A includes more demonstrations of results.

Now that we have a reliable model to extract the total nonlinear stiffness, we delve into the methodology to extract the nonlinear electrical and mechanical stiffness.

3.3 Non-Linear Electrical and Mechanical Stiffnesses (k_{e3} , k_{m3})

Recall that the linear electrical stiffness, k_{e1} , sprung out of the Taylor series expansion of $\frac{\partial C}{\partial r}$ (3). Therefore, we can express up to the m^{th} order electrical stiffness by taking up to the $(m - 1)$ term of (3). Doing so, generates the following electrostatic force:

$$F_{es,non-lin} = \frac{1}{2} \frac{\kappa_k C_{ok}}{d_o} \left(1 + \frac{2\kappa_k}{d_o} r + \frac{3\alpha_3}{d_o^2} r^2 + \frac{4\alpha_4}{d_o^3} r^3 \right) (V_P - v_i)^2 \quad (30)$$

With some algebraic manipulations, and leaving terms only at the frequency of v_i , the electrostatic force simplifies to:

$$F_{es,non-lin} \approx -\frac{\kappa_k v_i V_P C_{ok}}{d_o} + \frac{\kappa_k^2 V_P^2 C_{ok}}{d_o^2} r - \frac{6\alpha_3 V_P v_i C_{ok}}{d_o^3} r^2 + \frac{4\alpha_4 V_P^2 C_{ok}}{d_o^4} r^3 \quad (31)$$

The fourth term of (31) has a coefficient directly proportional to the third power of the radial motion of the device. Thus, the expression for the non-linear electrical stiffness, k_{e3} :

$$k_{e3k} = \frac{4\alpha_4 V_P^2 C_{ok}}{d_o^4} \quad (32)$$

and since the second order non-linearity drops off in the derivation of (28) we can ignore the second order nonlinear stiffness k_{e2} :

$$k_{e2k} = \frac{6\alpha_3 V_P v_i C_{ok}}{d_o^3} \quad (33)$$

To test the accuracy of (32), we extract the nonlinear stiffness as a function of the bias voltage and fit the data to:

$$k_3 = k_{m3} - \alpha_4 \frac{16V_P^2 C_o}{d_o^4} \quad (34)$$

as shown in Figure 9 where α_4 and k_{m3} serve as the fitting parameters. Note that we account for every single port's contribution to k_{e3} in (34).

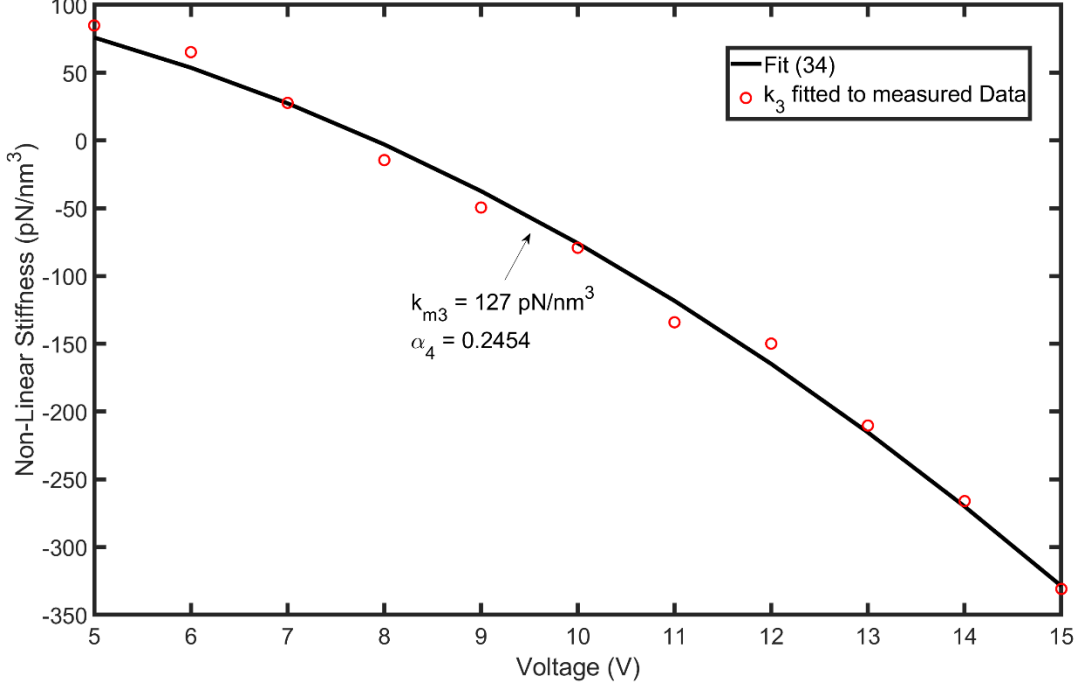


Figure 9: Non-Linear stiffness, k_3 , as a function of bias voltage, V_P

Interestingly, the value of α_4 (0.2454) is approximately that of κ_k^4 (0.2744). Which, strictly by observation, can lead us to believe the modification coefficients, α_n , introduced in (3) can take the form of κ_k^{n+1} . Providing motivation for future research into the validity of the claim:

$$\alpha_n = \kappa_k^{n+1} \quad (35)$$

Additionally, we can see from Figure 9 that the device experiences regions of spring stiffening ($k_3 > 0$) and spring softening ($k_3 < 0$) where the resonant peak bends toward the higher and lower frequencies respectively (Figure 10). We solve for the critical bias voltage, $V_{P_{crit}}$, that divides the two regions and eliminates non-linearities in the device by setting k_3 to zero and solving for V_P . The solution gives us:

$$V_{P_{crit}} = \frac{1}{4} d_o^2 \sqrt{\frac{k_{m3}}{\alpha_4 C_o}} \quad (36)$$

Once we plug in the different parameters $V_{P_{crit}}$ ends up being around 8 V for our case. Note that $V_{P_{crit}}$ is not dependent on the input power, therefore the device will operate linearly at all input powers if biased to $V_{P_{crit}}$. Of course, this is true given the device is not operating near breakdown (i.e. when the resonator contacts the electrodes). Hence (36) gives insight as to what design parameters serve as knobs to control the bias point of the device and thus maintain linearity. All of which, except for k_{m3} are readily available for the designer. Even though we don't have an analytical expression for k_{m3} , we intuitively know it is dependent on the geometry of the device, adding motivation for future research in discovering an analytical form for k_{m3} .

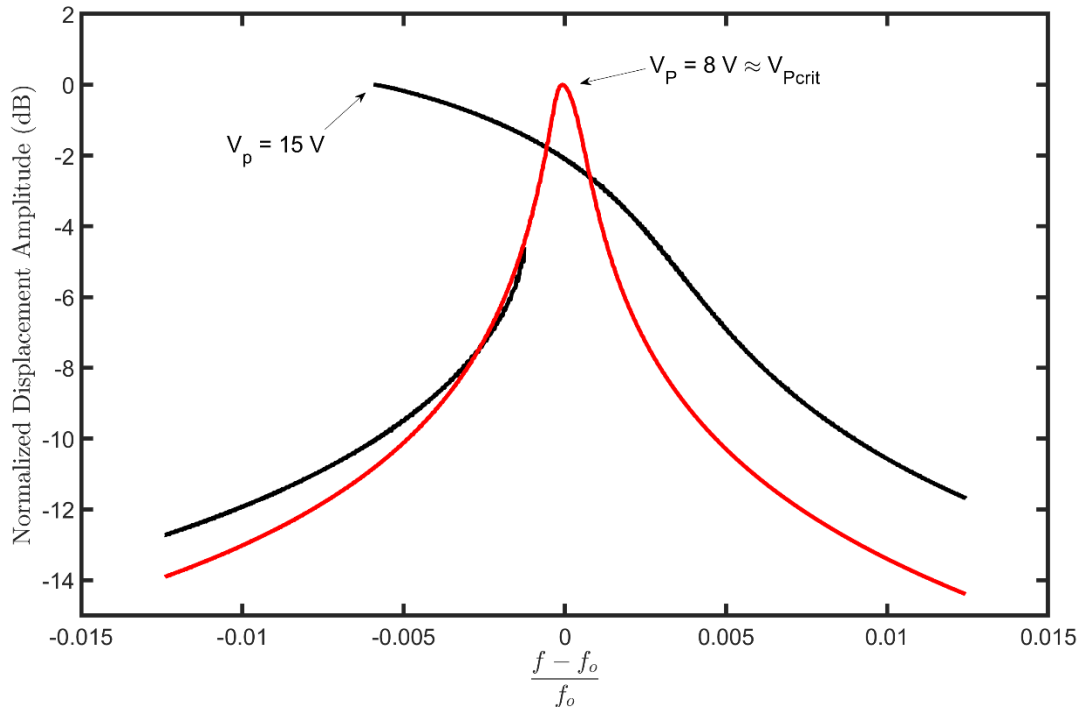


Figure 10: Normalized vibration amplitude with spring softening and nullification

Plotting the normalized displacement amplitude as a function of the fractional change in frequency from resonance allows us to isolate the softening and nullification effect of varying V_p . In doing so, we remove the frequency shift and effective electrical resistance change due to the variation in V_p .

Chapter 4: Conclusion

4.1 Achievements

The work presented in this report provides a reliable method to extract mechanical and electrical non-linear stiffnesses from typical device through measurements while simultaneously accurately modeling the non-linear vibrational response of the device. With the derived model we can easily predict how to nullify the overall non-linear stiffness by making use of the non-linear electrical stiffness' dependence on the bias voltage. Consequently, allowing design parameters to control the linearity of the device at high input powers. Specifically:

1. Derived an analytical model for the non-linear mode of operation in a WGD using the Harmonic Balance Method. Arriving at an accurate expression to predict the behavior of the device.
2. Derived and verified experimentally an expression for the non-linear electrical stiffness of a WGD. Also, extracted the mechanical stiffness of the WGD by fitting to said derived models.
3. Derived and verified experimentally an expression for the critical bias voltage that can nullify the non-linear effects caused by driving the device at high input powers.
4. Discovered the degradation of quality factor when the device is duffing, although theory suggests it should remain constant.

Overall, the models and expressions provided in this report can be incorporated into circuit models, such as in [6], to study how the duffing mode of operation effects the behavior of oscillators, channel select filters, and super-regenerative receivers (to name a few) that are composed of WGDs.

4.2 Future Research Directions

Although we have shown a derivation for a comprehensive model for the non-linear vibration of a WGD, we still cannot solve for the non-linear mechanical stiffness analytically. Thus, we should direct future efforts toward experimentation and finite element simulation to generate theory to predict the value of k_{m3} without having to extract it from data.

Additionally, one can verify the unsupported claim of (35) by measuring other WGDs designed with different electrode coverage angles to determine α_4 . If the trend continues to follow (35), more suitable theory, similar to that of [6], can be followed to determine the analytical expression.

Appendix A: Non-Linear Model Curve Fits

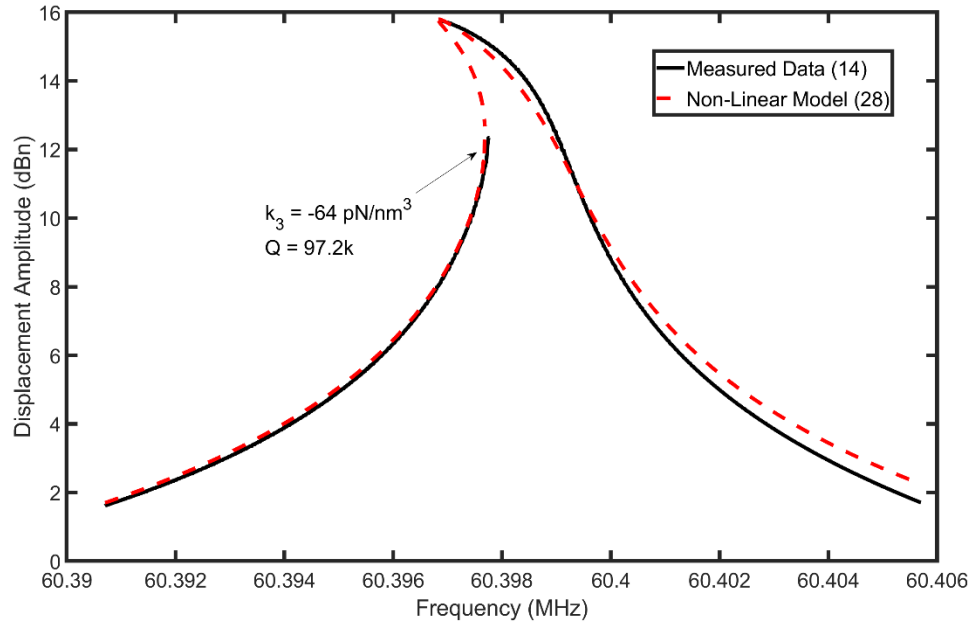


Figure 11: Non-linear measured data and model ($V_p = 9 \text{ V}$ and $P_{in,dBm} = -10 \text{ dBm}$)

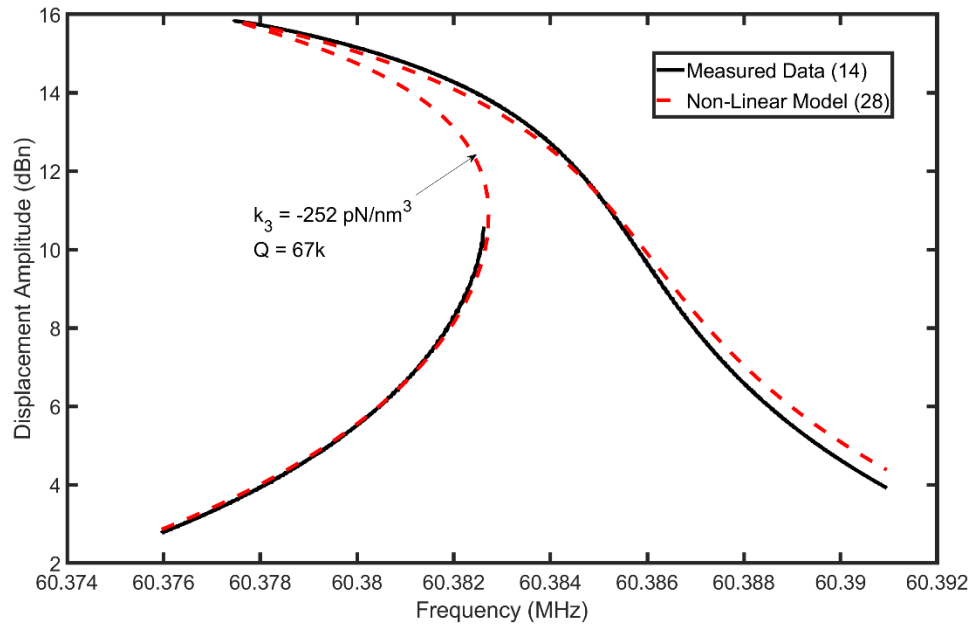


Figure 12: Non-linear measured data and model ($V_p = 13 \text{ V}$ and $P_{in,dBm} = -10 \text{ dBm}$)

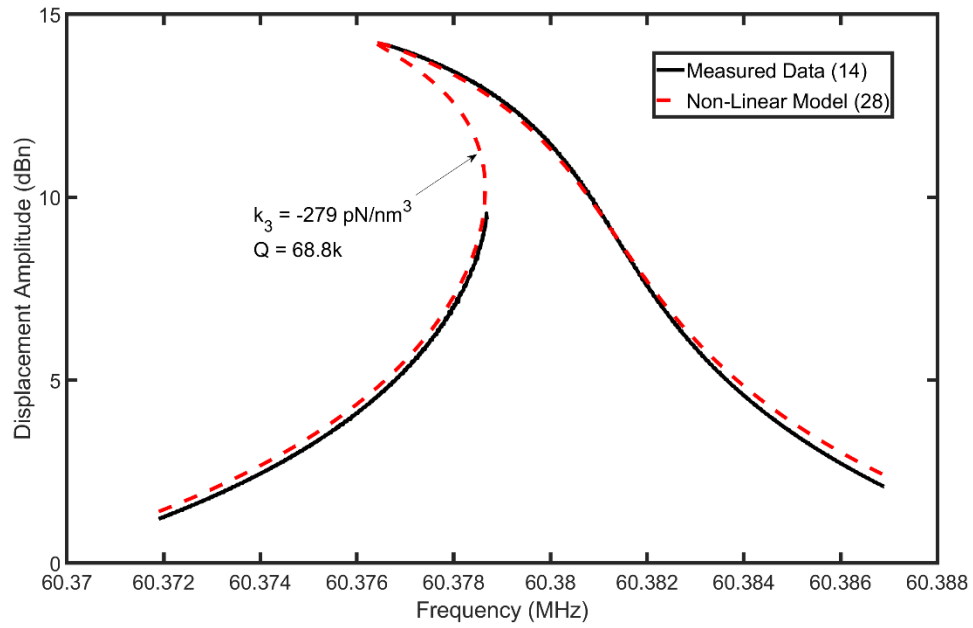


Figure 13: Non-linear measured data and model ($V_p = 14 \text{ V}$ and $P_{in,dBm} = -14 \text{ dBm}$)

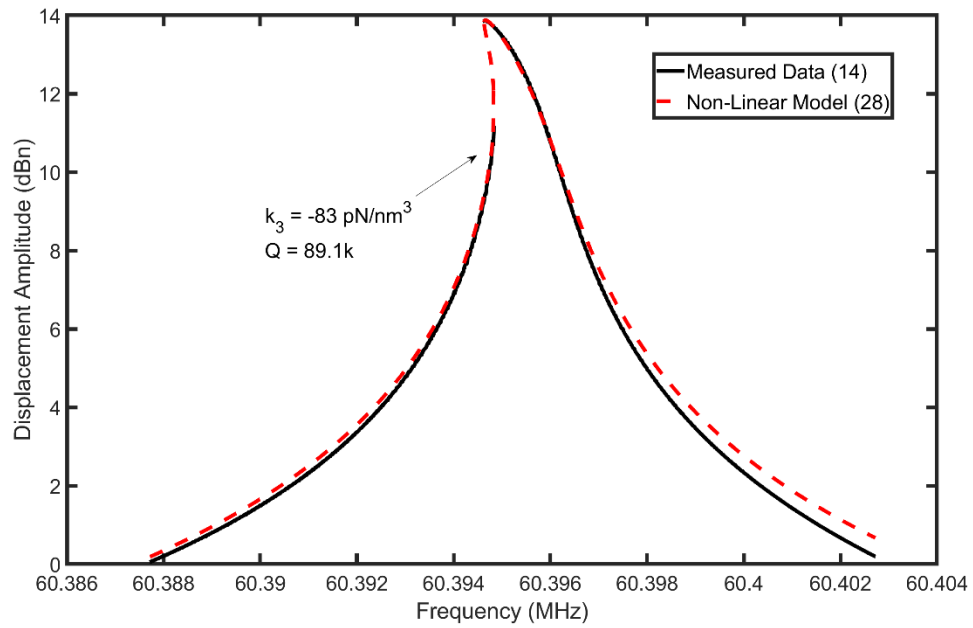


Figure 14: Non-linear measured data and model ($V_p = 10 \text{ V}$ and $P_{in,dBm} = -14 \text{ dBm}$)

References

- [1] P. M. R. Ruby, "Micromachined thin film bulk acoustic resonators," in *IEEE 48th Annual Symposium on Frequency Control*, 1994.
- [2] C. T. Nguyen, "MEMS Technology for Timing and Frequency Control," *IEEE Transactions on Ultrasonics, Ferroelectrics, and Frequency Control*, vol. 54, no. 2, pp. 251-270, 2007.
- [3] A. F. G. F. W. G. J. M. F. M. L. R. W. R. G. S. I. S. K. W. C.C.W. Ruppel | R. Dill, "SAW devices for consumer communication applications," *IEEE Transactions on Ultrasonics, Ferroelectrics, and Frequency Control*, vol. 40, no. 5, pp. 438 - 452, 1993.
- [4] J. H. J. K. R. R. B. O. A. Nelson, "A 22 μ W, 2.0GHz FBAR Oscillator," in *IEEE Radio Frequency Integrated Circuits Symposium*, Baltimore, 2011.
- [5] T. B. L. W. M. A. Z. R. T. O. R. a. C. T.-C. N. Thura Lin Naing, "2.97-GHz CVD Diamond Ring Resonator With Q >40,000," in *IEEE International Frequency Control Symposium*, Baltimore, 2012.
- [6] L. W. Z. R. C. T.-C. N. Mehmet Akgul, "A Negative-Capacitance Equivalent Circuit Model for Parallel-Plate Capacitive-Gap-Transduced Micromechanical Resonators," *IEEE Transactions on Ultrasonics, Ferroelectrics, and Frequency Control*, vol. 61, no. 5, pp. 849-869, 2014.
- [7] J. C. Lindenlaub, "An Approach for Finding the Sinusoidal Steady," in *Proc. 7th Ann. Allerton Conf. Circuit and Systems Thoery*, Chicago, 1969.
- [8] E. M. Baily, *Steady State Harmonic Analysis of Nonlinear Networks*, Stanford, 1968.
- [9] F. Bannon, J. Clark and C.-C. Nguyen, "High-Q HF microelectromechanical filters," *IEEE Journal of Solid-State Circuits* , vol. 35, no. 4, pp. 512-526, 2000.
- [10] C. T.-C. Nguyen, *Micromechanical Signal Processors*, Berkeley: University of California Berkeley, 1994.
- [11] J. Wang, Z. Ren and C.-C. Nguyen, "1.156-GHz Self-Aligned Vibrating Micromechanical Disk Resonator," *IEEE Transactions on Ultrasonics, Ferroelectrics, and Frequency Control*, vol. 51, no. 12, pp. 1607-1628, 2004.
- [12] S. G. M. R. G. e. a. Azizi, "Tuning the primary resonances of a micro resonator, using piezoelectric actuation," *Nonlinear Dynamics*, vol. 76, no. 1, pp. 839-852, 2014.

- [13] J. Y. S. K. C. L. X.L. Jia, "Resonance frequency response of geometrically nonlinear micro-switches under electrical actuation," *Journal of Sound and Vibration*, vol. 331, no. 14, pp. 3397-3411, 2012.
- [14] F. Y. M. & P. H. M. T. Tajaddodianfar, "Nonlinear dynamics of MEMS/NEMS resonators: analytical solution by the homotopy analysis method," *Microsystems Technologies*, vol. 23, no. 6, pp. 1913-1926, 2017.
- [15] R. M. S. C. J. S. S. Y. a. T. W. K. Hyung Kyu Lee, "Stable Operation of MEMS Oscillators Far Above the Critical Vibration Amplitude in the Nonlinear Regime," *Journal of Microelectromechanical Systems*, vol. 20, 2011.